Scoping Calculations on Leakage of CO_2 in Geologic Storage

Christine Doughty and Larry R. Myer

Earth Sciences Division

Lawrence Berkeley National Laboratory

Berkeley California

Numerical simulations have been carried out to evaluate the rate at which a plume of CO_2 moves upward through the subsurface, and the amounts of dissolution and phase trapping that occur along the way. A quantity of CO_2 is injected into a 1000-m deep, 100-m thick layer saturated with saline water, where it forms an immiscible supercritical fluid phase and partially dissolves in the aqueous phase. As the supercritical CO_2 moves upward, it smoothly transitions into a gas. Between the injection interval and the ground surface the medium (the "overburden") is assumed to be homogeneous, but anisotropic, with a ratio of vertical to horizontal permeability of 1:2. 1000-year simulations are conducted for overburden vertical permeabilities of 100 md, 10 md, and 1 md, using a version of the TOUGH2 numerical simulator that incorporates hysteretic relative permeability and capillary pressure functions. For each permeability, simulations are carried out for a range of maximum residual gas saturations ($S_{gr\max}$), because this parameter plays a key role in phase trapping and is poorly known for aqueous/CO_2 systems. The time required for the CO_2 plume to reach the surface increases with decreasing overburden permeability and increasing $S_{gr\max}$. CO_2 reaches the surface within 1000 years only for the highest overburden permeability (100 md), with times ranging from 775 years for the large values of $S_{gr\max}$ commonly used in the petroleum industry to 2.2 years for small values of $S_{gr\max}$. Additional simulations including a high-permeability conduit in an otherwise low-permeability overburden provide insights into the effects of geologic heterogeneity.

INTRODUCTION

Because of the very large quantities of CO_2 involved, a portfolio of approaches, including improved energy efficiency and energy production from renewables and other non-fossil sources, will be needed in order to stabilize atmospheric level of CO_2 [*Pacala and Socolow*, 2004]. Geologic storage, involving capture of CO_2 at large point sources such as power plants, cement plants and refineries, followed by transportation and injection into the deep subsurface, is another potential mitigation method. The primary targets for geologic storage will be sedimentary basins, and in particular, the porous, saline-saturated formations, oil and gas reservoirs, and deep, unmineable coals found in these basins. By far the largest storage capacity in sedimentary basins will be in the saline formations. There is great uncertainty in the volume of CO_2 which might be stored in saline formations, but it appears to be large, with the current estimate of world-wide storage capacity ranging from as little as 1000 Gt to possibly as much as 10^4 Gt CO_2 [*IPCC*, 2005].

Under almost all realistic injection scenarios, CO_2 will be less dense than the surrounding fluid in a saline saturated formation. This means that buoyancy will be a fundamental driving force for leakage of CO_2 from saline formation storage projects. Counteracting this driving force will be the resistance to upward flow provided by the permeability and capillary pressure characteristics of the rock layers, and the potential for the CO_2 to dissolve into the surrounding saline water and react with surrounding rock. In addition, as a finite plume migrates upward, imbibition of the wetting phase (water) will trap free phase CO_2.

This paper explores the fate of a finite plume of CO_2, which is injected into a porous saline saturated layer. The properties of the overburden were varied with the intention

of bounding what might be considered acceptable, average, overburden properties for a storage site. The model, however, is highly idealized, ignoring the effects of layers, heterogeneity, and structure, with the exception of a single through-going high permeability conduit. In addition, no reactions between the CO_2 and the rock are included in the calculations. Recent reactive transport modeling [*Xu et al*, 2003, 2005] suggests the effect of these reactions would be to further retard the rate of plume movement by reducing the mass of the free phase CO_2 and by reducing permeability through precipitation of reaction products.

IDEALIZED PROBLEM

The model for this study is shown in Figure 1. CO_2 is injected into a porous formation 100 m thick located at a depth of 1000 m. The porosity of the formation is 28%, horizontal permeability is 200 md, and vertical permeability is 100 md. An impermeable boundary is placed at the base of the model. Above the porous formation is an overburden, which extends to the surface. In three cases considered in this study, the overburden was assumed to have homogeneous properties. In one case, a single high-permeability channel extends from the porous layer through the overburden to the surface.

Table 1 provides the properties assumed for the overburden in the various simulations. The porosity and permeability values are typical of many clastic sedimentary rocks found throughout the world. Very little data is available on the multiphase flow properties of CO_2 and brine in clastic rocks. The present studies employ hysteretic functions based on the *van Genuchten* [1980] formulation, which are described in the "Numerical Simulator" section below. The parameters of the capillary pressure curves are adapted from mercury intrusion laboratory tests on core samples from the Frio formation [*S. Sakurai, personal communication*, 2004], an extensive sedimentary formation in the upper Texas gulf coast that is considered an attractive target for CO_2 sequestration, with capillary pressure strength $1/\alpha$ scaled by the square root of permeability. The *m* parameter of the relative permeability curves is chosen to make the van Genuchten curves resemble *Corey* [1954] curves, which are widely used to describe multiphase flow behavior in the petroleum literature. The S_{lr} and S_{grmax} values are taken from the literature.

Initially, the brine saturation is 100% everywhere in the model and a normal hydrostatic pore pressure gradient is assumed, with a pressure of 1 bar at the surface. A geothermal gradient of 30° C/ km is assumed, with the temperature at the surface and base of the model held constant at 15°C and 48° C, respectively. The salinity of the pore water is assumed to be 100,000 ppm.

Table 1. Overburden properties for various cases. Storage formation properties are those of the Case 1 overburden for all simulations. The Case 4 overburden consists of a central channel with properties of Case 1 emplaced in a overburden with properties of Case 3.

Property	Case 1	Case 2	Case 3
Porosity ϕ	0.28	0.22	0.16
Horizontal Permeability (md)	200	20	2
Vertical Permeability (md)	100	10	1
Relative Permeability Parameters			
m	0.917	0.917	0.917
S_{lr}	0.30	0.30	0.30
S_{grmax}	0.27	0.34	0.44
Capillary Pressure Parameters (same for drainage and wetting curves)			
$1/\alpha$ (bars)	0.133	0.421	1.33
n	1.7	1.7	1.7
S_{lmin}	0.03	0.03	0.03

The numerical simulations begin with injection of 900,000 tons of CO_2 into the porous formation. This quantity of CO_2 corresponds roughly to the emissions of a 1,000 MW coal fired power plant for 30 days. It is injected at a constant rate of 30,000 tons per day for 30 days. After injection stops, the only driving force in the model tending to cause movement of the CO_2 is buoyancy. Simulations continue for 1,000 years.

The numerical simulations were carried out using a 2D axisymmetric model composed of 61 layers each containing 41 grid blocks. All grid blocks are 20 m thick except for a few layers near the surface, which are thinner to better resolve surface arrival time. Radial grid block extent is 20 m out to a distance of 600 m, after which it steadily increases to produce an infinite-acting model.

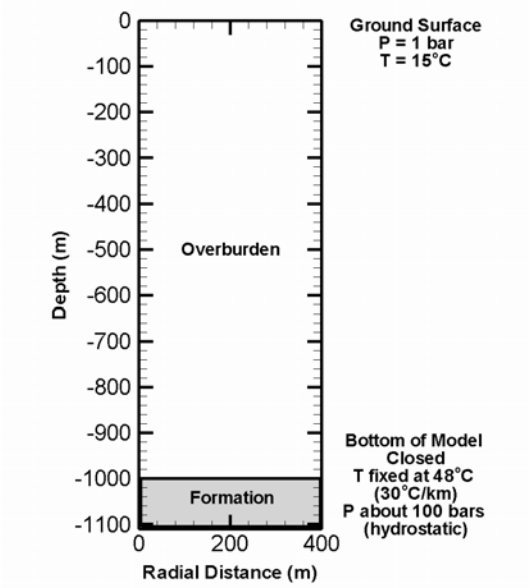

Figure 1. Schematic diagram of the axisymmetric model used for the numerical simulations.

PHYSICAL PROCESSES

The physical processes considered for the present problem consist of the multiphase, multicomponent flow of water, CO_2, and salt, along with heat flow. Water exists primarily in the liquid phase, salt may dissolve in the liquid water or precipitate as a solid, and CO_2 partitions between an immiscible phase and dissolution in the liquid water. Assuming a typical hydrostatic pressure gradient and geothermal temperature gradient, at typical CO_2 sequestration depths (>800 m below the surface), temperature and pressure conditions are well above the critical point, and the immiscible CO_2 is supercritical, as shown in the phase diagram in Figure 2. Figure 2 shows several typical paths from the 1000-m sequestration depth to the ground surface, As CO_2 moves upward toward the surface, if it remains in thermodynamic equilibrium with its surroundings, whether or not it crosses the saturation line depends on the surface temperature. For the larger of the two surface temperatures shown (path 2), immiscible CO_2 properties transition smoothly from supercritical to gas phase, as shown for density in Figure 3. These are the conditions considered in the present paper, and we always refer to the immiscible CO_2 as the gas phase, although it may in fact be supercritical.

Key factors impacting the effectiveness of CO_2 sequestration include buoyancy flow, geologic heterogeneity, multiphase interference, and dissolution of CO_2. At depths between the sequestration level and the ground surface, immiscible CO_2 is significantly lighter and less viscous than the surrounding brine, making it strongly buoyant. How much the CO_2 plume actually moves upward depends on the geologic structure and the intrinsic permeability of the rock. An anticline structure capped by a continuous low permeability shale effectively curtails upward movement (structural or stratigraphic trapping), but breaks in the shale layer or other geologic heterogeneity such as faults can provide preferential flow paths enabling extensive upward movement. The brine-bearing formations considered for CO_2 sequestration are typically water wet. That is, the native brine is the wetting phase and the immiscible CO_2 is the non-wetting phase. Thus the upward movement of an immiscible CO_2 plume includes both drainage at the leading edge of the plume where CO_2 displaces brine, and rewetting (imbibition) at the trailing edge of the plume where the water re-enters pore spaces. It is well established in the petroleum literature that the rewetting process can immobilize a significant fraction of the non-wetting phase, a process known as phase trapping. When CO_2 dissolves in liquid water it increases the density of the water slightly, thus eliminating the upward buoyant force on the CO_2 (dissolution trapping). A final means of effectively trapping CO_2, which is not considered in the present work, is through chemical reactions with rock minerals, which convert CO_2 into carbonate compounds (mineral trapping). Such processes are typically slow, but can ultimately result in a significant fraction of the CO_2 becoming immobilized [*Pruess et al.,* 2003].

NUMERICAL SIMULATOR

The numerical simulator used for the present work is TOUGH2, a general-purpose simulator for multiphase, multicomponent fluid flow through porous or fractured geologic media with heat transfer [*Pruess et al.,* 1999]. The equation of state package employed, ECO2 [*Pruess and Garcia,* 2002], considers water, CO_2, and NaCl. Thermodynamic conditions include super- as well as sub-critical CO_2, but for sub-critical conditions, ECO2 does not distinguish liquid and gaseous CO_2, and associated phase changes cannot be represented. Thus, ECO2 can model flow paths that resemble the right-hand path (path 2) shown in Figure 2, and do not cross the saturation line. This can be accomplished by choosing a relatively warm surface temperature to keep the geothermal gradient on the gas side of the saturation line, and considering slow enough flows so that the CO_2 plume remains in near thermodynamic equilibrium with its surroundings, and thus remains close to the geothermal gradient.

A new equation of state package for TOUGH2 called EOSM [*Pruess,* 2004] has recently been developed that considers the more general problem in which CO_2 may exist in the supercritical state, as a liquid, as a gas, or in various combinations of these three states, along with a rigorous phase-transition capability for crossing the saturation line. Simulation results using ECO2 were verified against those using EOSM to show that ECO2 produces correct results when the saturation line is not encountered. Simulation results using EOSM [*Pruess,* 2004] show that for rapid flow in which the CO_2 plume does not remain in thermodynamic equilibrium with its surroundings, the flow paths tend to be drawn toward the critical point and the saturation line. Such strong flows typically occur through a wellbore or along a localized fault. Here we are more concerned with bulk flow through the overburden as a whole, which tends to be much slower and hence amenable to the ECO2 approach.

TOUGH2 uses the integral-finite-difference method for spatial discretization [*Narasimhan and Witherspoon*, 1976]. For regular geometries this method is equivalent to a simple finite-difference method, whereas for complicated geometries it has all the flexibility of a finite element method. TOUGH2 solves fully coupled fluid flow and heat flow equations, using implicit time-stepping. The resulting discrete nonlinear algebraic equations for mass and energy conservation are written in a residual form, and solved using Newton/Raphson iteration.

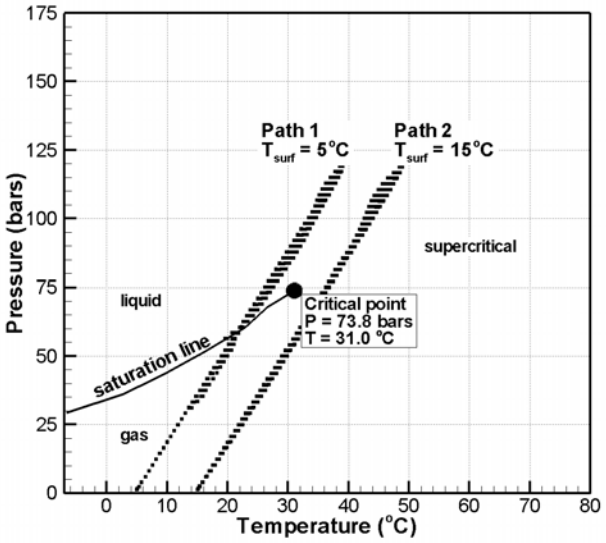

Figure 2. CO_2 phase diagram and two alternative paths from the sequestration depth to the ground surface.

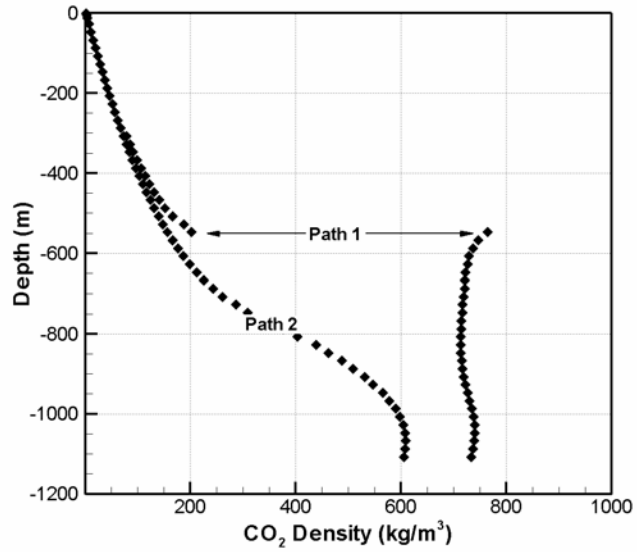

Figure 3. Density of CO_2 along two alternative paths from the sequestration depth to the ground surface.

Fluid flow is governed by a multiphase version of Darcy's law:

$$q_\beta = -\frac{k k_{r\beta} \rho_\beta}{\mu_\beta} (\nabla P_\beta - \rho_\beta g), \qquad (1)$$

where β denotes the phase (*l* for liquid, *g* for gas), q_β is the Darcy velocity (volumetric flow rate per unit cross-sectional area) of phase β, *k* is the intrinsic permeability of the medium, $k_{r\beta}$ is the relative permeability of phase β, ρ and μ are density and viscosity, respectively, of phase β, P_β is the pressure of phase β and *g* is the gravity force. The pressure of liquid and gas phases differ by the capillary pressure, P_c:

$$P_l = P_g + P_c . \qquad (2)$$

Together, capillary pressure and relative permeability are known as characteristic curves; they control the way the liquid and gas phases interact. We consider characteristic curves to be hysteretic functions of liquid saturation. That is, for a given grid block, P_c, k_{rl}, and k_{rg} depend not only on the saturation at that grid block, but the history of the saturation at that grid block. Some parameters within the characteristic curve functions depend only on the process (drainage or imbibition) that is occurring, so it is convenient to subdivide the characteristic curves into drainage curves and wetting curves. Other parameters depend on the value of the saturation when the grid block makes a transition from drainage to imbibition or vice versa, the so-called turning point saturations. Because turning-point saturations differ among all grid blocks, these parameters do as well. The most critical parameter in the latter category is the residual gas saturation, denoted S_{gr}^{Δ}, which is the saturation below which gas is immobile (i.e., the saturation below which immiscible CO_2 is trapped). Under drainage conditions, $S_{gr}^{\Delta} = 0$, but for imbibition, S_{gr}^{Δ} increases as the turning-point saturation between the drainage curve and wetting curve S_l^{Δ} decreases. Thus, grid blocks that once contained the most CO_2 are those which trap the most CO_2.

The simulations begin with a brine-saturated formation ($S_l = 1$) and inject immiscible CO_2, so as CO_2 reaches each grid block, multiphase flow begins using a P_c known as the primary drainage curve. Whenever liquid increases in a given grid block, a transition is made to a scanning wetting curve, which is interpolated between the primary drainage curve and the so-called primary wetting curve, using the value of S_l^{Δ}. If liquid saturation decreases again, a transition is made to a scanning drainage curve, again obtained by interpolation, which is followed until liquid saturation drops below its previous minimum value, S_l^{Δ}, at which point the primary drainage curve is again followed. A similar sequence of curve transitions occurs for other drainage-wetting-drainage-wetting scenarios. Several simple drainage-wetting paths are illustrated in Plate 1.

The primary drainage and primary wetting curves are based on the *van Genuchten* [1980] capillary pressure function

$$P_c = -\frac{1}{\alpha^\gamma}\left[\left(\frac{S_l - S_{l\min}}{1 - S_{gr}^{\Delta} - S_{l\min}}\right)^{-\left(\frac{n^\gamma}{n^\gamma - 1}\right)} - 1\right]^{(1/n^\gamma)}, \quad (3)$$

where γ denotes the branch (*d* for drainage, *w* for wetting) of the capillary pressure curve and α, $S_{l\min}$, and *n* are fitting parameters. For both primary and scanning drainage curves, $S_{gr}^{\Delta}=0$. For scanning wetting curves, S_{gr}^{Δ} is given by a modified version of the well-known *Land* [1969] equation as

$$S_{gr}^{\Delta} = \frac{(1 - S_l^{\Delta})}{1 + [1/S_{gr\max} - 1/(1 - S_{lr})](1 - S_l^{\Delta})}, \quad (4)$$

where S_{lr} is the residual liquid saturation (the saturation below which the liquid phase is immobile, assumed to be a constant rock property), S_l^{Δ} is the turning-point saturation for the transition from the primary drainage curve to the first-order wetting scanning curve, and $S_{gr\max}$ is taken as a function of porosity ϕ, obtained by fitting a wide range of sandstone data from the petroleum literature [*M. Holtz, personal communication*, 2002; *Holtz,* 2005]

$$S_{gr\max} = -0.3136 * \ln(\phi) - 0.1334. \quad (5)$$

Note in Equation (4) that when $S_l^{\Delta} = S_{lr}$ (corresponding to as complete a drainage of the medium as possible), $S_{gr}^{\Delta} = S_{gr\max}$ and that when $S_l^{\Delta} \sim 1$ (only slight drainage before wetting begins), $S_{gr}^{\Delta} \sim 0$.

Details of the interpolation procedure used to determine the scanning drainage and wetting curves are not reproduced here; they are based on the dependent domain theory of *Mualem* [1984], and their implementation in TOUGH2 is fully described in *Finsterle et al.* [1998] and *Niemi and Bodvarsson* [1988].

The relative permeability functions also include hysteretic effects arising from the trapped component of the gas phase that develops during wetting. These functions are taken from *Parker and Lenhard* [1987] and *Lenhard and Parker* [1987], who adapted them from the non-hysteretic expressions of *van Genuchten* [1980]. As implemented in TOUGH2, the relative permeability functions are

$$k_{rl} = \sqrt{\bar{S}_l}\left[1 - \left(1 - \frac{\bar{S}_{gt}}{1 - \bar{S}_l^{\Delta}}\right)(1 - (\bar{S}_l + \bar{S}_{gt})^{1/m})^m - \left(\frac{\bar{S}_{gt}}{1 - \bar{S}_l^{\Delta}}\right)(1 - (\bar{S}_l^{\Delta})^{1/m})^m\right]^2 \quad (6)$$

$$k_{rg} = (1 - \bar{S}_l - \bar{S}_{gt})^{1/3}(1 - (\bar{S}_l + \bar{S}_{gt})^{1/m})^m, \quad (7)$$

where $\bar{S}_l$ and $\bar{S}_l^{\Delta}$ are effective values of liquid saturation S_l and turning point liquid saturation S_l^{Δ}, respectively, normalized with respect to irreducible liquid-phase saturation S_{lr}:

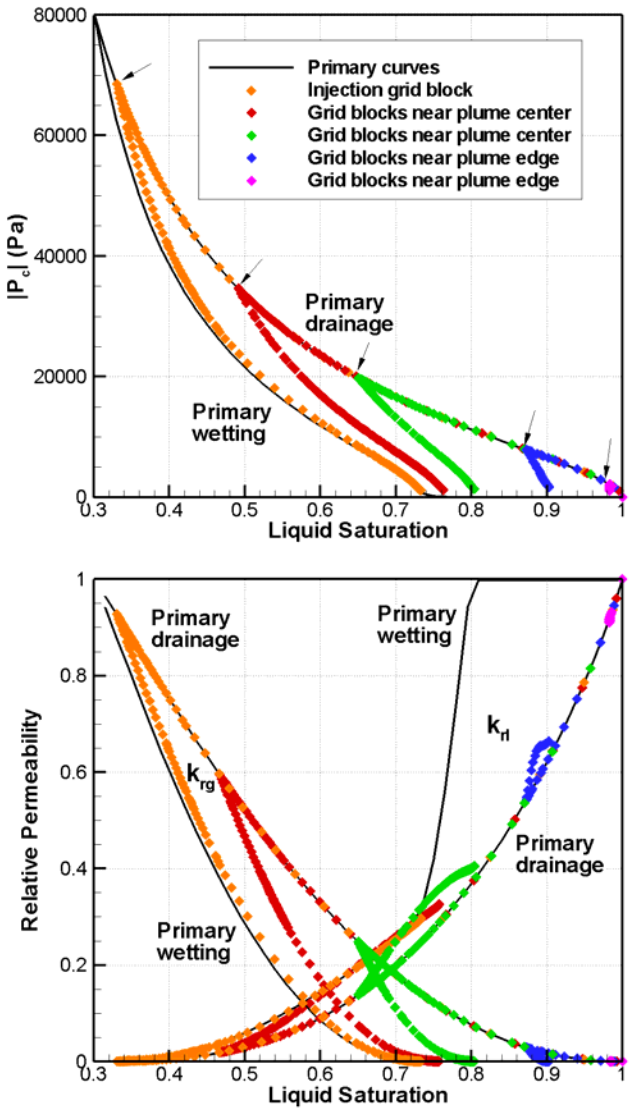

Plate 1. Hysteretic capillary pressure (top) and relative permeability (bottom) paths for several locations within an injected CO_2 plume. All paths begin at $S_l = 1$ along the primary drainage curve; the transition to a wetting scanning curve occurs at S_l^{Δ} (shown by arrows); as $|P_c| \to 0$ on the wetting curves, $S_l \to (1 - S_{gr}^{\Delta})$.

$$\overline{S}_l = \frac{S_l - S_{lr}}{1 - S_{lr}} \tag{8}$$

$$\overline{S}_l^{\Delta} = \frac{S_l^{\Delta} - S_{lr}}{1 - S_{lr}} . \tag{9}$$

The parameter $\overline{S}_{gt}$ is the effective value of the trapped gas phase, which is given by

$$\overline{S}_{gt} = \frac{S_{gr}^{\Delta}(S_l - S_l^{\Delta})}{(1 - S_{lr})(1 - S_l^{\Delta} - S_{gr}^{\Delta})} . \tag{10}$$

Relative permeability paths for several locations within a CO_2 plume are shown in Plate 1.

Until recently, the hysteretic version of TOUGH2 has not been numerically efficient enough to be used for 2D or 3D CO_2 sequestration problems. Recent modifications have improved the numerics, however, making it competitive with non-hysteretic simulations. The first key modification is to ensure that P_c, k_{rl}, and k_{rg} functions are continuous and differentiable within and beyond the turning-point saturations and S_{gr}^{Δ} that nominally limit their domain. This is required because actual saturations may fall outside this domain due to dissolution of CO_2 or numerical effects. Secondly, an option to delay curve switching to the end of each time step has been added. This has the effect of making the fully implicit time-stepping routine normally employed by TOUGH2 partially explicit.

SIMULATION RESULTS

A suite of simulations of the idealized CO_2 plume emplacement and evolution problem were carried out, considering four cases for overburden properties, as given in Table 1. Because values of $S_{gr\max}$ are taken from the petroleum literature, and it is not known just how applicable they are to brine/CO_2 systems, for each overburden permeability, four different values of $S_{gr\max}$ were considered: the original value taken from the literature (denoted "large"), and three other values, denoted "medium", "small", and zero. A value of $S_{gr\max} = 0$ is not physically realistic, but it is useful for illustrating limiting behavior. Table 2 summarizes the main results of all the simulations. The four numbers shown for each simulation are $S_{gr\max}$, the time CO_2 reaches the ground surface t_{surf}, the time at which all CO_2 becomes immobile t_{im}, and the time at which more CO_2 is dissolved than is in the immiscible phase t_{dis}. Case 4D does not run successfully, because large focused flow up the central conduit does not remain in thermodynamic equilibrium with the surrounding geothermal temperature gradient and is drawn too close to the critical point for the ECO2 equation of state to be valid. In the subsequent paragraphs, selected results from the Table 2 simulations will be shown and discussed, followed by graphical representations of the dependence of the three time measures on overburden properties.

Table 2. Simulation results showing $S_{gr\max}$ for each case along with the time to reach the surface t_{surf}, time to immobilization t_{im}, and time at which more CO_2 is dissolved than free phase t_{dis} (all times in years).

Case	Overburden permeability	Overburden $S_{gr\max}$ A. Large (Eq. 5)	B. Medium	C. Small	D. Zero	
1	200/100 md	0.27	0.15	0.05	0	$S_{gr\max}$
		775	53	2.2	1.7	t_{surf}
		10	30	300	N/A	t_{im}
		500	6	0.7	0.6	t_{dis}
2	20/10 md	0.34	0.20	0.10	0	$S_{gr\max}$
		>1000	>1000	>1000	>1000	t_{surf}
		30	100	300	N/A	t_{im}
		>1000	100	6	4	t_{dis}
3	2/1 md	0.44	0.30	0.15	0	$S_{gr\max}$
		>1000	>1000	>1000	>1000	t_{surf}
		100	300	1000	N/A	t_{im}
		>1000	60	21	20	t_{dis}
4	200/100 md conduit in 2/1 md overburden	0.27&0.44	0.15&0.30	0.05&0.15	Too close to critical point	$S_{gr\max}$
		2.3	2.2	2.2		t_{surf}
		100	300	1000		t_{im}
		>1000	26	10		t_{dis}

Plates 2 through 5 show results for case 1A, which has a 100 md vertical permeability and a large value of S_{grmax}. Plate 2 shows a time series of spatial distributions of free-phase CO_2 (denoted S_g for gas saturation, although below a depth of 800 m, the CO_2 is supercritical). For this large vertical permeability the leading edge of the CO_2 plume moves readily upward, but the large value of S_{grmax} ensures that a significant portion of the CO_2 remains close to the injection depth.

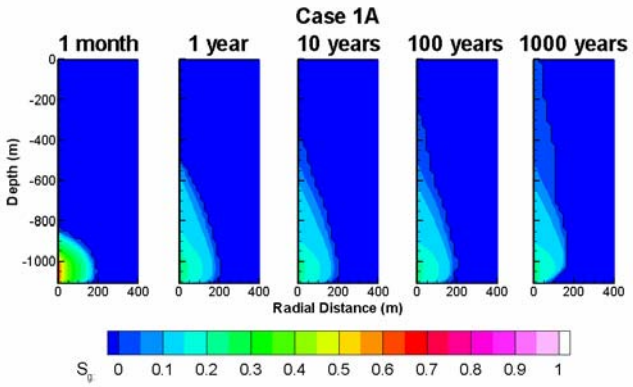

Plate 2. Free-phase CO_2 distributions at a series of times for Case 1A. The single contour line shows $S_g = 0$.

Plate 3 shows a time series of the variable that identifies which branch of the capillary pressure curve is being followed: the primary drainage curve, the first-order wetting scanning curve, the second-order drainage scanning curve, or the third-order wetting scanning curve. At one month (the end of the injection period), the entire plume is draining. At one year, most of the plume is wetting (the 3-month plot would have shown the top half of the plume draining and the bottom half wetting). At late times, the dominance of higher-order scanning curves indicates that saturation changes are small and tend to be oscillatory, as the bulk of the plume becomes immobile.

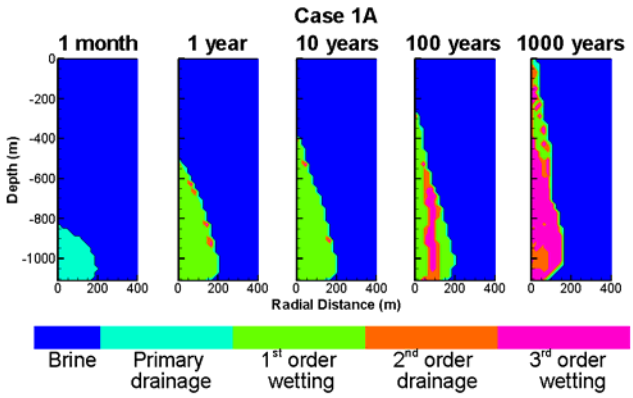

Plate 3. Capillary pressure curve distributions at a series of times for Case 1A. The single contour line shows $S_g = 0$.

Plate 4 shows a time series of spatial distributions of S_{gr}^{Δ}. Comparison with Plate 2 indicates that much of the plume is immobile by 1 year.

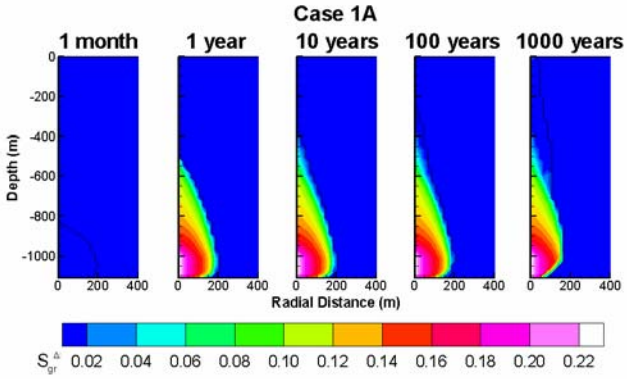

Plate 4. Residual gas saturation S_{gr}^{Δ} at a series of times for Case 1A. The single contour line shows $S_g = 0$.

Plate 5 shows a time series of spatial distributions of temperature. At early times when the plume is localized there is a marked temperature decrease close to the well accompanying the expansion of CO_2 into the formation. Farther away, temperature increases due to the heat produced by CO_2 dissolution.

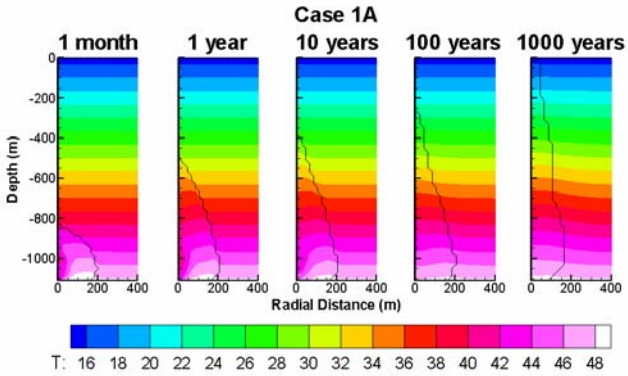

Plate 5. Temperature at a series of times for Case 1A. The single contour line shows $S_g = 0$.

The top frame of Figure 4 presents a mass balance for the model as a whole for Case 1A, giving an integrated picture of the fate of the CO_2 through time. The aqueous (dissolved) and immiscible (free-phase) fractions sum to the total, whereas the mobile and immobile fractions sum to the immiscible fraction. Each mass fraction is then normalized to the amount of CO_2 originally injected into the model. Although the plume reaches the surface at t_{surf} = 775 years, the amount of CO_2 escaping is so small that is does not show on the plot. The immiscible fraction of CO_2 steadily decreases as the plume moves upward, contacts new brine, and partially dissolves, with the aqueous fraction showing a complementary increase. The time at

which more CO_2 is dissolved than free phase is t_{dis} = 500 years. Within the immiscble phase, the mobile fraction steadily declines and the immobile fraction steadily increases until the bulk of the plume is immobilized at t_{im} = 10 years. As shown in Plate 2, the leading edge of the plume continues to move upward after t_{im}, but Figure 4 indicates that the fraction of mobile CO_2 is extremely small.

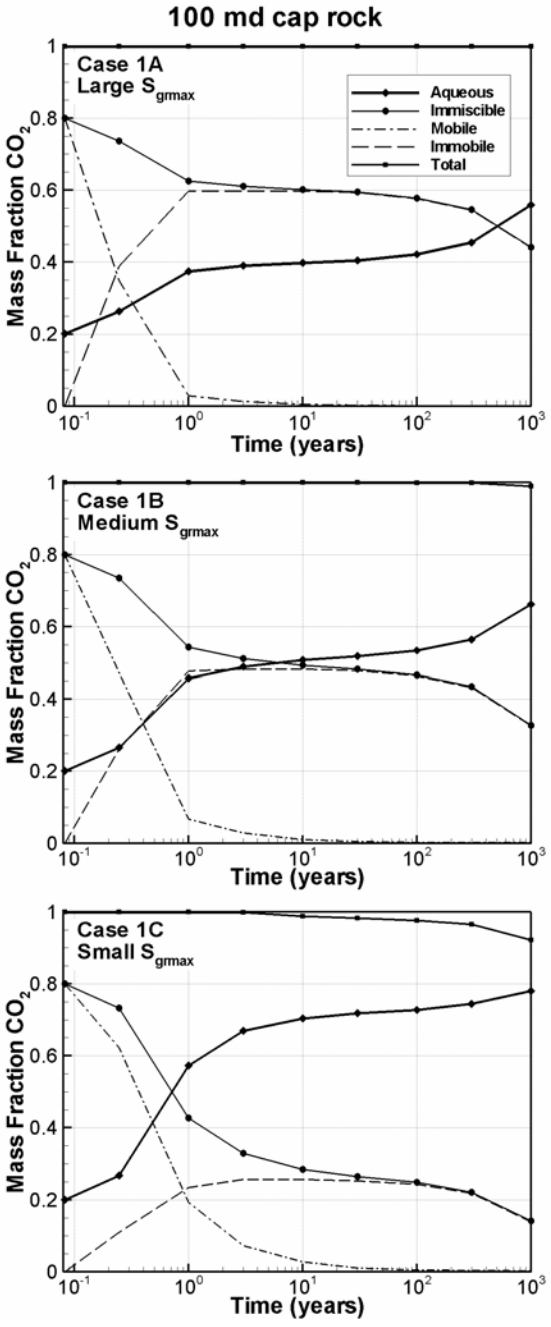

Figure 4. Mass balances for Cases 1A, 1B, and 1C.

Plate 6 shows a time series of free-phase CO_2 distributions for Cases 1B and 1C, a 100 md overburden with medium and small values of $S_{gr\max}$, respectively. For this high permeability, decreasing $S_{gr\max}$ enables much greater upward flow. Figure 4 shows the mass balances for these two cases. As $S_{gr\max}$ gets smaller, the plume reaches the surface sooner (t_{surf} = 775 years for Case 1A, 53 years for Case 1B and 2.2 years for Case 1C) and remains mobile longer (t_{im} = 10 years for Case 1A, 30 years for Case 1B, and 300 years for Case 1C). The time at which more CO_2 is dissolved than free-phase also gets shorter as $S_{gr\max}$ decreases (t_{dis} = 500 years for Case 1A, 6 years for Case 1B, and 0.7 years for Case 1C), due to the greater mobility of the plume bringing it into contact with more brine, hence enabling more dissolution. These trends for t_{im} and t_{dis} also hold for the lower permeability overburden cases.

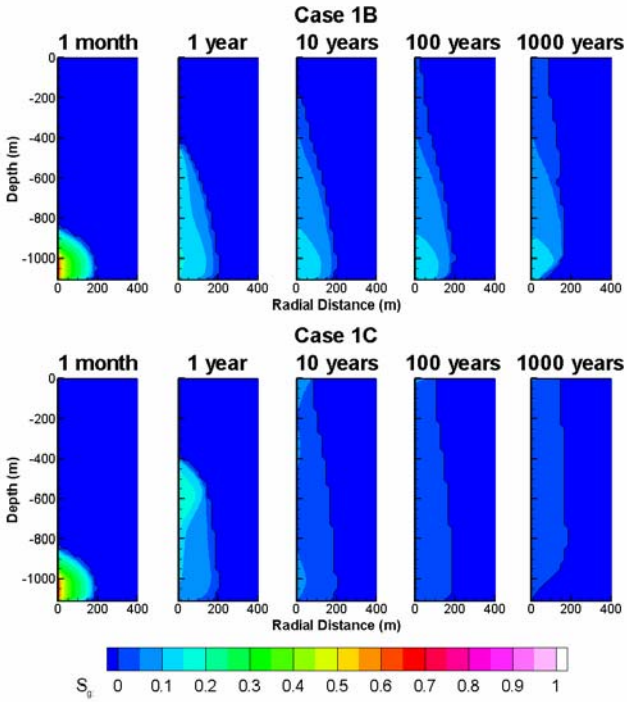

Plate 6. Free-phase CO_2 distributions at a series of times for Cases 1B (top) and 1C (bottom). The single contour line shows S_g = 0.

Plate 7 shows a time series of free-phase CO_2 distributions for Cases 2A and 2C, a 10 md overburden with large and small values of $S_{gr\max}$, respectively. With a factor of ten decrease in overburden permeability compared to Case 1, the character of the plume evolution changes drastically. The leading edge of the plume moves up only a few hundred meters within 1,000 years, even when $S_{gr\max}$ is small. Plate 8 shows the analogous plots for Cases 3A and 3C, a 1 md overburden with large and small values of $S_{gr\max}$, respectively. For these cases, upward movement is extremely limited.

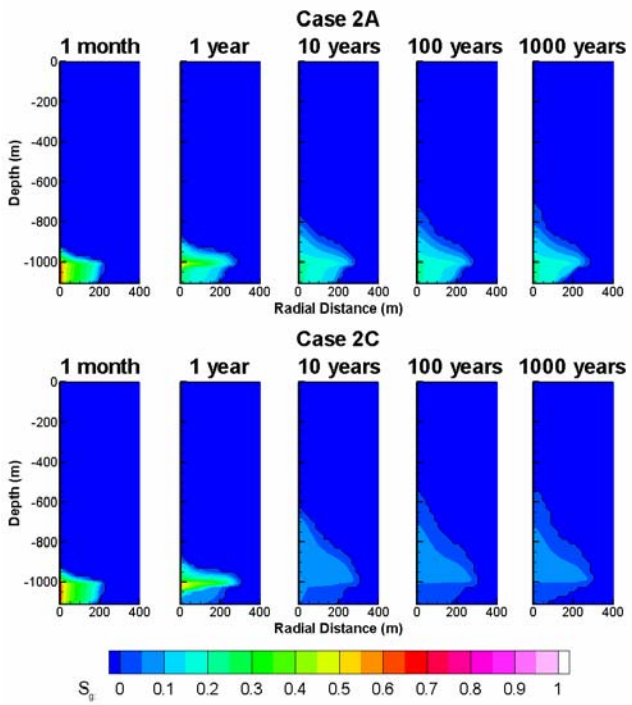

Plate 7. Free-phase CO_2 distributions at a series of times for Cases 2A (top) and 2C (bottom). The single contour line shows $S_g = 0$.

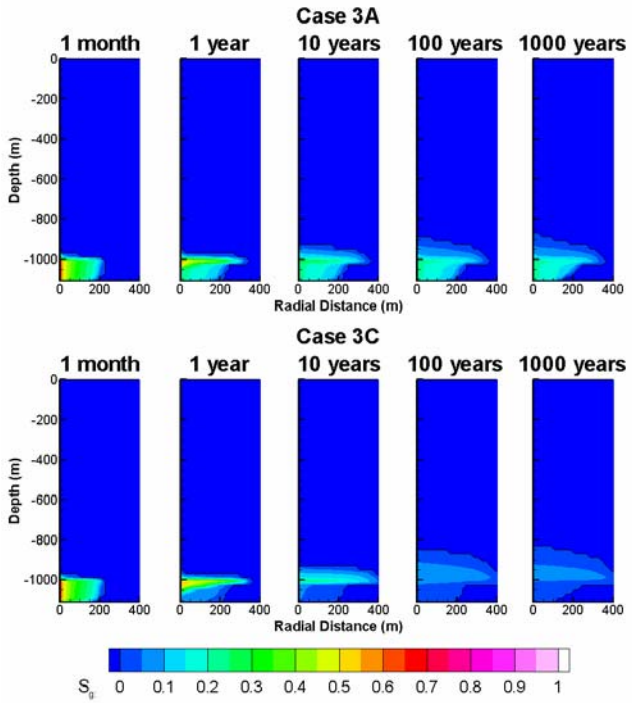

Plate 8. Free-phase CO_2 distributions at a series of times for Cases 3A (top) and 3C (bottom). The single contour line shows $S_g = 0$.

Figures 5 and 6 shows the mass balance plots for Cases 2 and 3, respectively. For both cases the trends of increasing t_{im} and decreasing t_{dis} with decreasing $S_{gr\max}$ observed for Case 1 are repeated. Comparing mass balances for different permeabilities (Figures 4, 5, and 6) shows another trend: as overburden permeability decreases, t_{im} and t_{dis} both tend to increase. This is because with lower permeability the CO_2 plume remains more compact, thus S_g decreases more slowly - leading to larger t_{im}, and less brine is in contact with immiscible CO_2 - leading to larger t_{dis}.

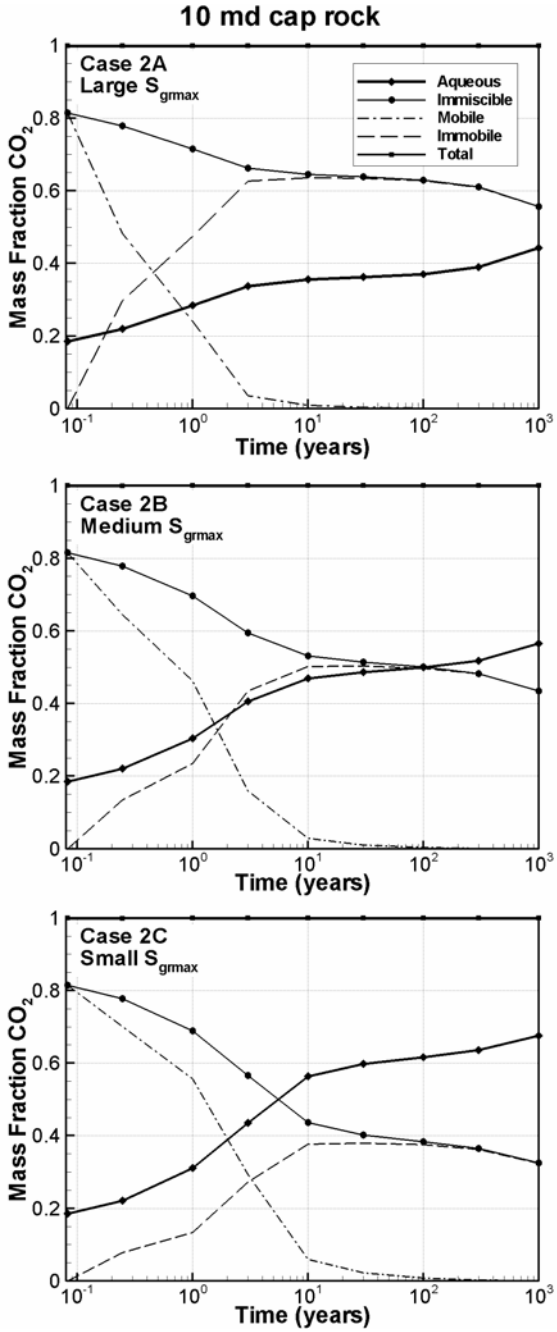

Figure 5. Mass balances for Cases 2A, 2B, and 2C.

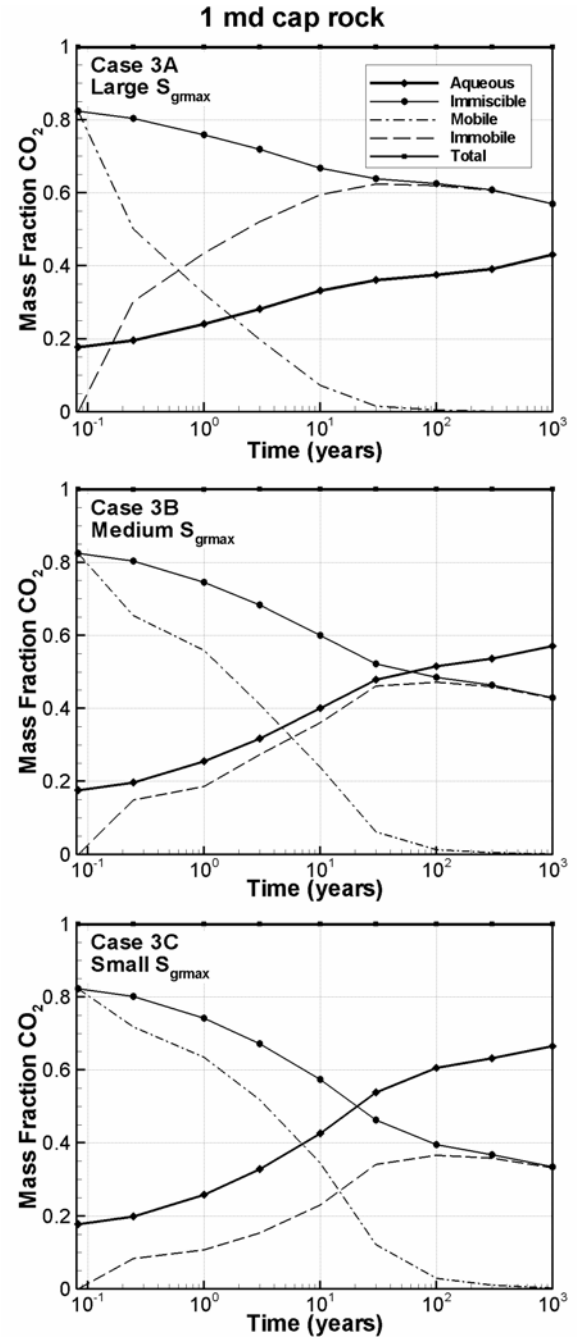

Figure 6. Mass balances for Cases 3A, 3B, and 3C.

Plate 9 graphically summarizes the dependence of all three time measures t_{surf}, t_{im}, and t_{dis}, on overburden permeability and S_{grmax}. As permeability decreases, t_{surf} increases (more stratrigraphic trapping) but both t_{im} and t_{dis} also increase (less phase and dissolution trapping). As S_{grmax} increases, t_{surf} increases and t_{im} decreases (more phase trapping), but t_{dis} increases (less dissolution trapping).

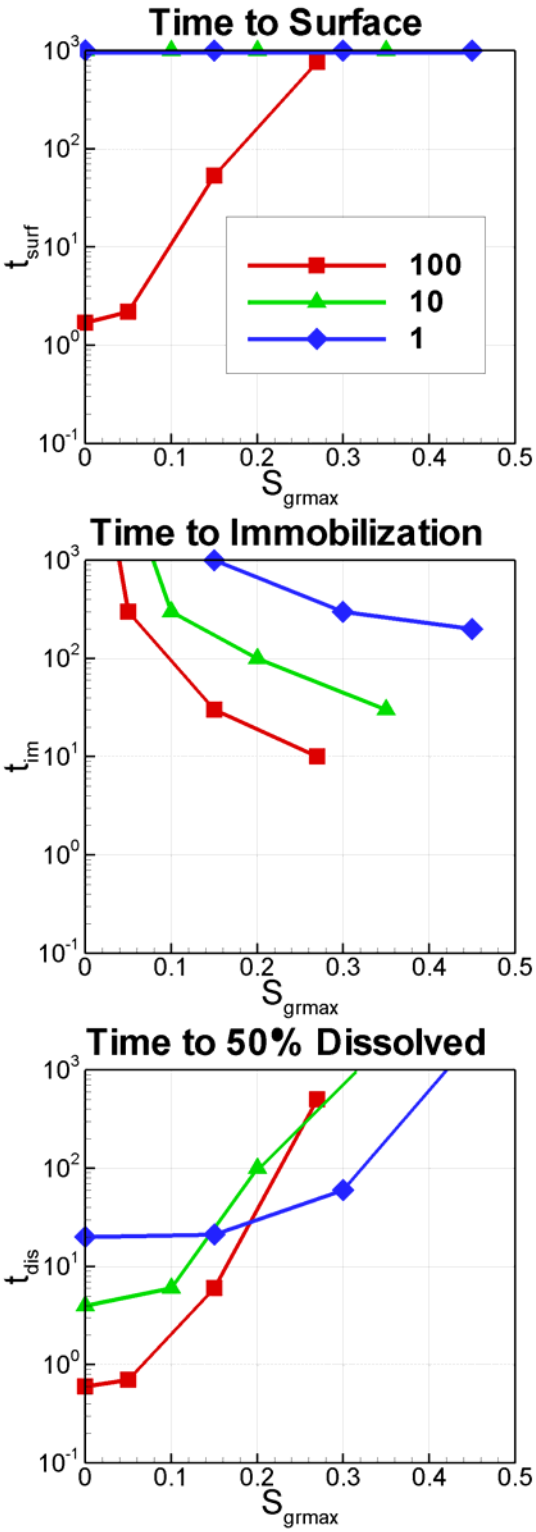

Plate 9. Summary of the effects of overburden permeability and S_{grmax} on time measures t_{surf}, t_{im}, and t_{dis}. Curves show results for different overburden permeabilities in md: Case A – 100, Case B – 10, Case C – 1.

In addition to the previous cases, which considered a homogeneous overburden, one additional case considering a simple heterogeneity was simulated. Case 4 contains a 35-m-radius cylindrical conduit at the center of the plume with a vertical permeability of 100 md, while the remainder of the overburden has a vertical permeability of 1 md. Plate 10 shows the free-phase CO_2 distributions for large and small values of $S_{gr\max}$. For the large value of $S_{gr\max}$, CO_2 arrives at the surface much earlier than for an overburden with a uniform vertical permeability of 100 md (t_{surf} = 2.3 years for Case 4A compared to 775 years for Case 1A). This early arrival reflects a combination of effects. For the uniform overburden, the high vertical permeability allows large upward flow of CO_2, but it also allows the plume to spread out, decreasing S_g and therefore trapping a large fraction of the CO_2, which greatly slows upward plume movement. In contrast, for the non-uniform overburden, the high vertical permeability conduit again allows large upward flow of CO_2, but now the flow is focused into this conduit and spreading is much less, therefore S_g does not decrease nearly as much and far less CO_2 is trapped, enabling the early surface arrival.

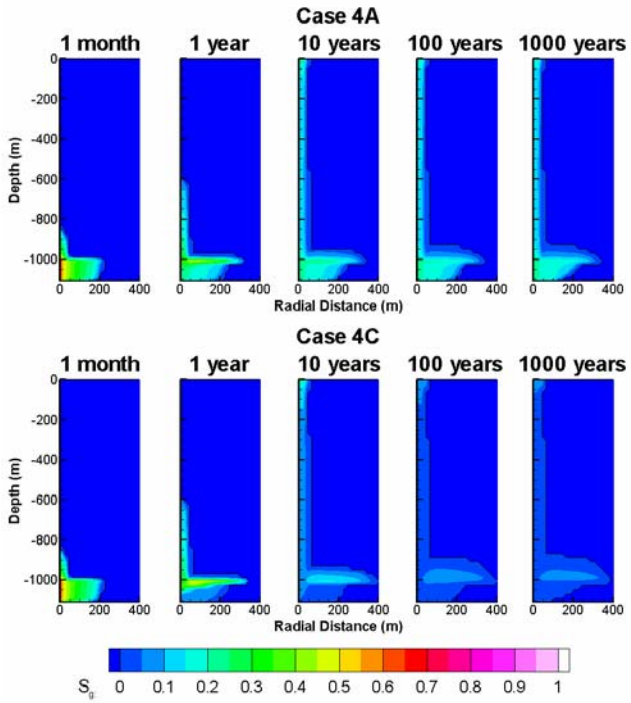

Plate 10. Free-phase CO_2 distributions at a series of times for Cases 4A (top) and 4C (bottom). The single contour line shows $S_g = 0$.

For the small value of $S_{gr\max}$ with minimal phase trapping, both uniform (Case 1C) and non-uniform (Case 4C) overburdens produce similar early surface arrivals (t_{surf} = 2.2 years), reflecting similar rates of flow through the 100 md portion of the overburden. Interestingly, for Case 4, t_{surf} is nearly the same for large and small values of $S_{gr\max}$, indicating that for the focused flow resulting from geologic heterogeneity, the leading edge of the plume (which controls t_{surf}) and the trailing edge of the plume (where phase trapping occurs) act essentially independently.

Figure 7 shows the mass balance plots for Case 4. In addition to the larger fraction of CO_2 lost to the surface compared to the uniform overburden case, t_{im} and t_{dis} are larger here, as the focused flow keeps S_g large longer, delaying t_{im}, and limits the amount of brine contacting free-phase CO_2, delaying t_{dis}.

SUMMARY, CONCLUSIONS, AND FUTURE WORK

Preliminary scoping calculations of an idealized CO_2 storage scenario have been conducted to examine the upward migration of an injected plume of CO_2, using a version of the numerical simulator TOUGH2 that includes a hysteretic formulation for capillary pressure and relative permeability. Results show that in the absence of high-permeability conduits, CO_2 reaches the surface within 1000 years only for the highest overburden permeability (100 md). It is noted that a permeability of 100 md is representative of a good reservoir, so a rock with such a permeability would never be considered to be a true "cap rock" (i.e., an upper confining layer). In fact, many reservoirs are developed in rock of 10 md permeability, and simulations with a 10-md overburden showed that the CO_2 failed to reach the surface within 1000 years.

Our scoping calculations also show that there are trade-offs between three key mechanisms for CO_2 trapping: stratigraphic trapping, phase trapping, and dissolution trapping. Low overburden permeability promotes stratigraphic trapping, but hinders phase and dissolution trapping by keeping the CO_2 plume compact. In contrast, high overburden permeability enables the plume to move upward more readily, but the attendant spreading promotes phase and dissolution trapping. A large value of $S_{gr\max}$ promotes phase trapping, but hinders dissolution trapping by minimizing contact between brine and free-phase CO_2.

Geologic heterogeneity is found to play a key role through a combination of the above mechanisms. Preferential flow paths through higher-permeability zones enhance upward migration to the surface, while the focused character of the flow hinders the spreading that enhances phase and dissolution trapping, enabling CO_2 to reach the surface sooner. Thus, characterizing overburden heterogeneity should be an important component of site-characterization studies for potential CO_2 storage projects.

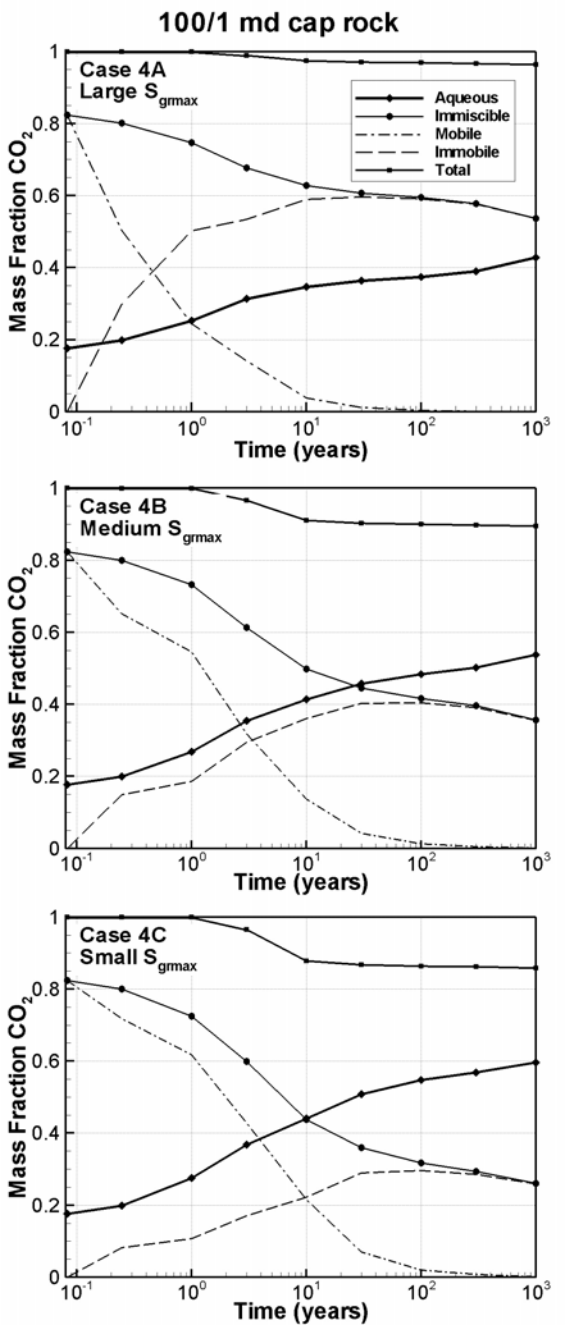

Figure 7. Mass balances for Cases 4A, 4B, and 4C.

These preliminary calculations have raised a number of interesting questions to motivate further work in this area. First, it will be necessary to incorporate a complete set of phase transitions including liquid, gas, and supercritical CO_2 along with brine in order to examine larger, faster upward CO_2 flows that do not remain in thermodynamic equilibrium with the geothermal gradient. Additionally, the present calculations do not include liquid-phase diffusion or gravity-driven flow of CO_2-saturated brine. Both effects are expected to be slow and act to improve CO_2 trapping.

Generalization from a 2D axisymmetric model to a fully 3D model will enable more realistic geologic heterogeneity to be considered, as well as the possibility of regional groundwater flow, which could greatly enhance contact between brine and free-phase CO_2, increasing dissolution trapping.

Finally, there remains much uncertainty as to what are appropriate multiphase flow properties (characteristic curves) for brine/CO_2 systems. As more information from laboratory and field tests becomes available, further simulations can be conducted. In the meantime, simulations that consider a range of parameter values for uncertain properties provide useful guidance for prioritizing lab and field efforts.

ACKNOWLEDGMENTS

Reviews by Karsten Pruess and Sally Benson of Lawrence Berkeley National Laboratory are appreciated. This work was supported by the Assistant Secretary for Fossil Energy, Office of Coal and Power Systems, through the National Energy Technology Laboratory, of the U.S. Department of Energy under Contract No. DE-AC02-05CH1123.

REFERENCES

Corey, A.T. The interrelation between gas and oil relative permeabilities, *Producers Monthly*, 38-41, November 1954.

Finsterle, S., T.O. Sonenborg, and B. Faybishenko, Inverse modeling of a multistep outflow experiment for determining hysteretic hydraulic properties, in K. Pruess, ed., Proceedings of the TOUGH workshop '98, *Rep. LNBL-41995*, Lawrence Berkeley National Laboratory, Berkeley, Calif., 1998.

Holtz, M. H., Reservoir characterization applying residual gas saturation modeling, example from the Starfak T1 reservoir, middle Miocene Gulf of Mexico, M.Sc. Thesis, University of Texas at Austin, 2005.

IPCC Special Report on Carbon Dioxide Capture and Storage, http://www.unep.ch/ipcc/activity/srccs/, 2005.

Land, C.S., Calculation of imbibition relative permeability for two- and three-phase flow from rock properties, *SPE Journal*, 9, 149-156, June 1969.

Lenhard, R.J. and J.C. Parker, A model for hysteretic constitutive relations governing multiphase flow, 2. Permeability-saturation relations, *Water Resources Research*, 23(12), 2197-2205, 1987.

Mualem, Y., A modified dependent domain theory of hysteresis, *Soil Science*, 137(5), 283-291, 1984.

Narasimhan, T.N. and P.A. Witherspoon, An integrated finite difference method for analyzing fluid flow in porous media, *Water Resources Research*, 12(1), 57-64, 1976.

Niemi, A. and G.S. Bodvarsson, Preliminary capillary hysteresis simulations in fractured rocks, Yucca Mountain, Nevada, *Journal of Contaminant Hydrology*, 3, 277-291, 1988.

Pacala, S. and R. Socolow, Stabilization wedges: Solving the climate problem for the next 50 years with current technologies, *Science*, 305, 968-971, 2004

Parker, J.C. and R.J. Lenhard, A model for hysteretic constitutive relations governing multiphase flow, 1. Saturation-pressure relations, *Water Resources Research*, 23(12) 2187-2196, 1987.

Pruess, K., Numerical simulation of CO_2 leakage from a geologic disposal reservoir, including transitions from super- to sub-critical conditions, and boiling of liquid CO_2, *SPE Journal*, 44, 237-248, June 2004.

Pruess, K. and J. García, Multiphase flow dynamics during CO2 disposal into saline aquifers, *Environmental Geology*, 42, 282-295, 2002.

Pruess, K., C. Oldenburg, and G. Moridis, TOUGH2 user's guide, version 2.0, *Rep. LBNL-43134*, Lawrence Berkeley National Laboratory, Berkeley, Calif., 1999.

Pruess, K., T. Xu, J. Apps, and J. García, Numerical modeling of aquifer disposal of CO_2 (SPE 83695), *SPE Journal*, 43, 49-60, March 2003.

Van Genuchten, M. Th., A closed-form equation for predicting the hydraulic conductivity of unsaturated soils, *Soil Science Society of America Journal*, 44(5), 892-898, 1980.

Xu, T., J. Apps, and K. Pruess, Reactive geochemical transport simulation to study mineral trapping for CO_2 disposal in deep Arenaceous formations, *J. Geophys. Res.* 108 (B2), 2003.

Xu, T., J. Apps, and K. Pruess, Mineral sequestration of carbon dioxide in a sandstone-shale system, *Chemical Geology*, 217, 295-318, 2005.

C. Doughty and L. Myer, Earth Sciences Division, Lawrence Berkeley National Laboratory, #1 Cyclotron Rd, MS 90-1116, Berkeley, CA 94702